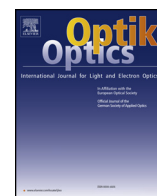




Contents lists available at ScienceDirect

Optik

journal homepage: www.elsevier.com/locate/ijleo

Original research article

Detection method of manufacturing defects on aircraft surface based on fringe projection



Renbo Xia^{a,b,*}, Jibin Zhao^{a,b}, Tianyu Zhang^{a,b}, Run Su^{a,c}, Yueling Chen^{a,b}, Shengpeng Fu^{a,b}

^a State Key Laboratory of Robotics, Shenyang Institute of Automation, Chinese Academy of Sciences, Shenyang 110016, China

^b Institutes for Robotics and Intelligent Manufacturing, Chinese Academy of Sciences, Shenyang 110169, China

^c University of Chinese Academy of Sciences, Beijing 100049, China

ARTICLE INFO

Keywords:

Fringe projection
Aircraft surface
Phase error
Rivet recognition

ABSTRACT

For high-value aircraft, in order to ensure their stealth, pneumatic and safety characteristics, surface geometric defects such as unacceptable rivet height and seam width must be accurately detected during the manufacturing process. These defects need to be controlled within a very small scope of error. Traditional defect detection methods are difficult to meet the actual requirements of manufacturing of advanced aircrafts in terms of information dimension, detection accuracy and efficiency. In this paper, a new method of high-precision 3D defect detection for controlling riveting and seam quality is proposed. For the complexity of illumination distribution on aircraft surface, first, an accurate surface measurement method based on fringe projection is proposed. Then, based on two-dimensional and three-dimensional information, a method of automatic identification and location of rivets and seams is developed. Finally, a visualization method based on augmented reality is proposed to help improve the operator's work efficiency. The experimental results show that the method has high detection accuracy and practicability.

1. Introduction

1.1. Background

The surface of the aircraft is mainly composed of skin surrounding the skeleton of fuselage and wing, whose surface manufacturing quality has a significant impact on the stealth, aerodynamic characteristics, flight safety and energy consumption of the aircraft [1–5]. Therefore, it is necessary to strictly detect the surface defects in the process of aircraft manufacturing. The indicators for evaluating the quality of the aircraft's surface manufacturing include: the unevenness of the rivet, the height and width differences between the adjacent skins at the butt joint [6–11]. Fig. 1 shows some typical surfaces of aircraft from which it can be clearly seen that the skin surfaces are covered with many rivets and seams.

For a long time, the manufacturing quality of aircraft surface is mainly detected by touching, caliper, plug ruler and other traditional methods. These methods can only roughly judge whether the measured object is qualified, and it is difficult to accurately describe the true size of defect, and also inconvenient for data archiving. Moreover, this type of contact measurement method is slow and inefficient. With the continuous improvement of product design requirements and machining accuracy, traditional measurement

* Corresponding author at: State Key Laboratory of Robotics, Shenyang Institute of Automation, Chinese Academy of Sciences, Shenyang 110016, China.

E-mail address: xiarb@sia.cn (R. Xia).

<https://doi.org/10.1016/j.ijleo.2020.164332>

Received 7 August 2019; Received in revised form 19 January 2020; Accepted 28 January 2020
0030-4026/ © 2020 Elsevier GmbH. All rights reserved.

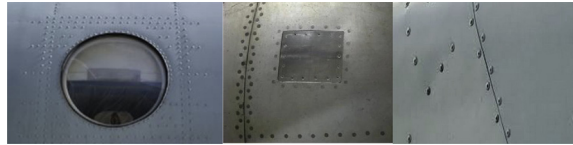


Fig. 1. Aircraft skin surface.

methods are increasingly difficult to meet the actual needs of aircraft surface defect detection. At present, there is an urgent need for a fast, non-contact, and digital method for surface manufacturing quality detection.

1.2. Related works

In 1988, Aloha Airlines Flight 243 suffered a serious flight accident due to the oxidation of the seams on the surface of the aircraft [12]. Since then, Carnegie Mellon University [6] has established a robotic laboratory for remote detection of aircraft skins, and has developed a series of wall-climbing robots for aircraft skin detection. This kind of robot can carry various non-destructive testing equipment to detect fatigue damage cracks, corrosion, pits and other defects on the surface of aircraft skin, but these studies still focus on two-dimensional detection, which can only judge whether the features exist or not, and cannot meet the needs of aircraft surface manufacturing quality detection. In 2006, Zheng Liu et al. [7] used Edge of Light (EOL) images to study the bump detection caused by the corrosion around the surface of aircraft skin, and proposed a rivet detection algorithm based on phase consistency. The algorithm has good robustness and can accurately locate rivets on aircraft surface. However, because it requires uniform rivet distribution and needs to know the number of rivets in each row in advance, which limits its use. In order to achieve rapid testing of aircraft surfaces, Boeing has developed a non-destructive testing device based on ultrasonic scanning [8], which is mainly used to complete surface scratches, internal cracks and corrosion detection. The system can scan the measured surface independently, which improves the automation of quality detection. However, due to the need to diagnose the test results manually, it is impossible to achieve full automation detection. In addition, the system is mainly aimed at the detection of cracks and corrosion, and cannot complete the judgment of height difference and gap width. Based on Optical Coherence Tomography technology, James H et al. [9] developed a hand-held aircraft rivet assembly quality inspection system, which can realize rapid measurement of rivet region flatness, radius and inclination angle. Since the device can only measure one rivet area at a time, the workload will be very large for an aircraft with several hundred thousand rivets. Therefore, the low measurement efficiency is the biggest drawback of the system.

At the 5th World Aerospace Nondestructive Testing Symposium held in 2013, Creaform Corporation of Canada [10] demonstrated an aircraft surface pit detection system based on the combination of structured light scanning and industrial close-range photogrammetry. By using a structured light scanner called Handyscan, the complete point cloud data of the aircraft surface can be obtained and analyzed to determine the locations and sizes of damage regions. However, the damage location obtained by the system can only be displayed on the computer screen. In order to find the physical location of the damaged area on the aircraft surface, it is very inconvenient for the inspector to compare the actual damage area of the aircraft with the damage area indicated by the computer screen, especially when the measured object is relatively large.

1.3. Contribution

The main contribution of this paper is to propose a method for aircraft surface manufacturing quality detection based on fringe projection, which mainly focuses on the two important defects: riveting and seam. The main contributions are as follows: a phase-shifting error control method is proposed to ensure the accurate measurement of aircraft non-uniform reflector surface; a new method for accurate identification and positioning of the rivet and the seam is developed; and a visualization method of aircraft surface manufacturing quality detection results is proposed.

The structure of the paper is as follows: Section 2 gives the principle of fringe projection measurement and error control method. In Section 3, a method of recognizing rivet area and seam area is proposed. In Section 4, the geometric analysis method based on point cloud data is discussed. And Section 5 gives a visualization method of the measurement results. In Section 6, an aircraft surface manufacturing quality detection system is developed and verified by experiments. Finally, Section 7 gives a summary and future work. The overall algorithm flowchart is shown as Fig.2.

2. Fringe projection measurement principle

Fringe projection technology, also known as surface structured light measurement technology, is an important method to achieve high-precision measurement of the surface with weak texture. The fringe projection measurement technology can obtain large-area dense point clouds at a time, which is better than line structure light in terms of efficiency and precision. Since the binocular structure has more constraints than the monocular system, the binocular fringe projection device is more accurate than the monocular device and has been widely studied and applied.

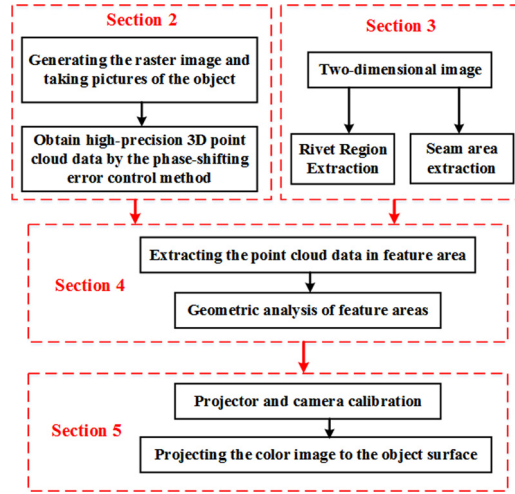


Fig. 2. Overall algorithm flowchart.

2.1. System setup

The measurement system [13] used in this paper is shown in Fig. 3. It is based on an active stereo photogrammetric setup with two cameras and a projector. After calibrating the intrinsic and external parameters of the two cameras, if the corresponding image points have been identified based on absolute phase map, the three-dimensional shape information of the object can be obtained by triangulation. The absolute phase map can be obtained by projecting several phase shifted sinusoidal stripe patterns. With the help of the epipolar geometry, the corresponding points are determined by finding image points with the same absolute phase value on the corresponding epipolar lines. Therefore, the measurement accuracy is highly dependent on the accuracy of the phase map.

2.2. Four-step phase-shifting algorithm

The analysis and experimental testing in this paper were carried out using the four-step phase-shifting algorithm which is commonly used in phase-shifting measurement systems. At the beginning, we assume that the projector and cameras have linear intensity response. The intensity of the fringe pattern projected from the projector can be expressed as

$$I^P(x, y) = a \cos[\phi(x, y)] + b \quad (1)$$

where a is the intensity modulation, b is the background intensity, and $\phi(x, y)$ is the desired phase information at coordinate (x, y) . Both a and b are the constant values. Let $r(x, y)$ represent the surface reflectivity at coordinate (x, y) and $b_1(x, y)$ be the ambient light that shines on the surface. Then the reflected light intensity can be expressed as

$$I^O(x, y) = r(x, y)[I^P(x, y) + b_1(x, y)] \quad (2)$$

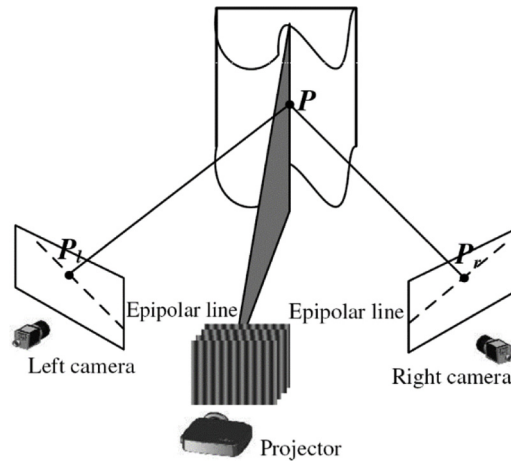


Fig. 3. Schematic diagram of the phase-shifting measurement system.

For four-step phase-shifting algorithm

$$I_i^o(x, y) = r(x, y)\{a \cos[\phi(x, y) + (i - 1)\pi/2] + b + b_1(x, y)\} \quad (3)$$

where $I_i^o(x, y)$ is the reflected light intensity of the i 'th fringe patterns with a phase shift of $(i - 1)\pi/2$. Then $\phi(x, y)$ can be solved as follows

$$\phi(x, y) = \tan^{-1} \left(\frac{I_4^o - I_2^o}{I_1^o - I_3^o} \right) \quad (4)$$

The phase map $\phi(x, y)$ is wrapped by 2π due to the arctangent function, and a three-frequency heterodyne principle can be used for full-field phase-unwrapping to obtain a continuous phase map.

For fringe projection measurement technology, the accuracy of phase calculation directly affects the accuracy of three-dimensional reconstruction. Generally, errors mainly come from: the non-linear response of projection and acquisition equipment, the non-uniform optical characteristics of the object surface, and the phase decoding method [14–17], etc. The projector and camera used in this paper is linearly responsive, so the phase error caused by the nonlinear response of the projector and camera does not need to be considered. For an object with free-form surface such as an aircraft, due to the incomplete controllability of ambient light in the measurement environment, its surface usually presents non-uniform reflection. In the region with high reflectivity, pixel saturation is easy to occur, resulting in large phase errors. Although it is possible to avoid saturation of these regions by reducing the aperture and exposure time, it also causes the low intensity in the weak reflectance region, which also causes a large phase error. Therefore, it is necessary to suppress the phase error caused by the non-uniform surface reflection. This paper adopts the author's previous method which has been proven to be very practical to control the phase error. More introduction and analysis can be found in previous work [13].

3. Image-based feature region recognition

There are a large number of rivets and seams on the surface of the aircraft skin. The assembly accuracy of these two features reflects the level of manufacturing quality of aircraft surface to a certain extent. This section mainly focuses on the identification and positioning methods of rivets and seams. Since the theoretical height difference between the rivet and the substrate surface is very small, it is difficult to perform rivet detection directly from the point cloud data. In addition, it takes more time to detect rivets in a point cloud. Therefore, we propose to locate the rivets and seams in the image, and then obtain the spatial position of the rivets and seams according to the mapping relationship between the image points and the spatial points.

3.1. Rivet extraction

After perspective projection, rivets on aircraft surface will be mapped to ellipses in the image. Then, the extraction of rivet will be transformed into the extraction of ellipse in the image. Due to the surface colors of the rivets and the background are very close, and the signal-to-noise ratio is relatively low, which makes it very challenging to accurately extract the ellipses of rivets from the image.

Ellipse extraction methods can be mainly divided into edge tracking based algorithms [18–20] and Hough transform based algorithms [21–23]. The edge tracking based algorithm is more efficient, but often find the wrong combination of elliptical arcs. The Hough transform based algorithm has very high recognition accuracy, but its computational complexity and memory consumption are large. Obviously, these two algorithms have their own advantages and disadvantages, and the reasonable approach is to learn from each other, that is, the edge tracking-based algorithm will be used to quickly extract the dominant edges in the image and pick out high-confidence rivets and suspect rivets, and then the algorithm based on the Hough transform is then used to identify suspected rivets. This method can avoid traversing the image using Hough transform-based algorithms. Therefore, the method proposed in this paper can quickly and robustly extract rivets in images. More detailed analysis and verification can be found in our previous work [24].

3.2. Seam extraction

The seam of the aircraft surface is a linear feature, and the grayscale of the seam in image is significantly lower than the grayscale of the skin on both sides of it. Therefore, the seam extraction can be converted into the extraction of the salient linear feature in the image. In this paper, the classic Steger algorithm [25,26] is used to extract the seam centerline. The main steps of the algorithm are as follows:

- (1) Extracting the seam center line by using the Steger algorithm;
- (2) Extracting straight line segments by using the Ransac method;
- (3) Merging straight line segments belonging to the same seam.

4. Geometric analysis of feature regions

In order to evaluate the manufacturing quality of the rivet and the seam, after extracting their feature area from the image, the

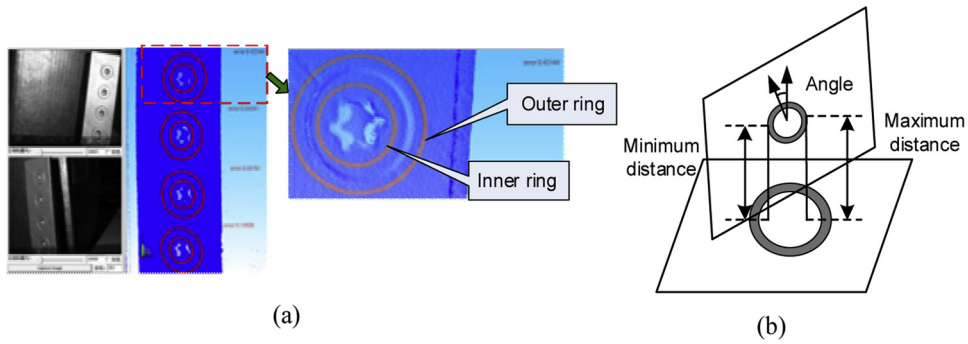


Fig. 4. Geometric analysis of rivet.

(a) Two sets of annular points collected on the inner and outer surfaces of the rivet; (b) Schematic diagram of angle and flatness calculation.

next step is to quantitatively analyze the three-dimensional geometry of their feature area based on point cloud data. For the rivet it is necessary to analyze the height difference and angle between its inner surface and the outer substrate surface. For the seam, the width and height difference across the gap need to be calculated.

4.1. Geometric analysis of rivet

The radius of curvature of the aircraft surface is relatively large, so a small area of it can be approximated by a plane. Therefore, the inner surface and the outer substrate surface of the rivet can be characterized by planes respectively. As shown in Fig. 4(a), two annular point clouds are extracted inside and outside the rivet, and then they are fitted into two planes by RANSAC algorithm, called the inner plane and the outer plane respectively, as shown in Fig. 4(b). The angle deviation of riveting can be expressed as the angle between the inner plane and the outer plane. The riveting flatness can be measured by the minimum height difference, the maximum height difference, and the average height difference from the point on the inner plane to the outer plane.

4.2. Geometric analysis of seam

The seam width and the height difference between its two sides are two important indicators for measuring the manufacturing quality of the aircraft surface. The flowchart of the seam geometric analysis method proposed in this paper is shown in Fig. 5.

First, the seam center line l^c is extracted from the image by using the method of Section 3.2. Assuming that q_0 is an inquiry point located on the line l^c . Therefore, a straight line l^q parallel to l^c and spaced apart by d_w can be constructed, as shown by the red line in Fig. 6, where d_w is the width of the seam. According to the correspondence between the image pixels and the reconstructed 3D points in the fringe projection measurement method, the corresponding spatial coordinates of each image pixels on l^q can be obtained and

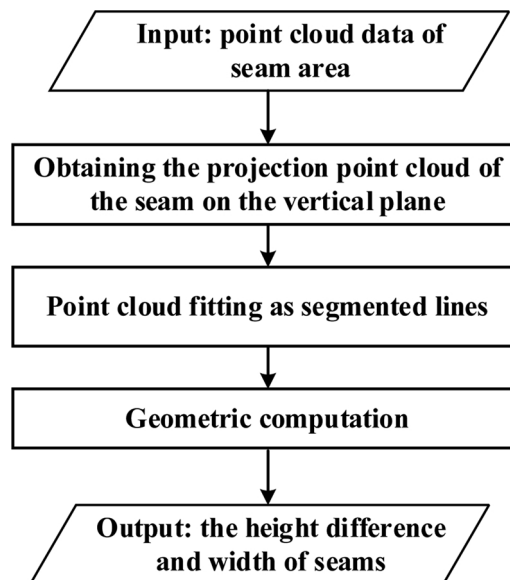


Fig. 5. Flowchart of the seam geometric analysis.

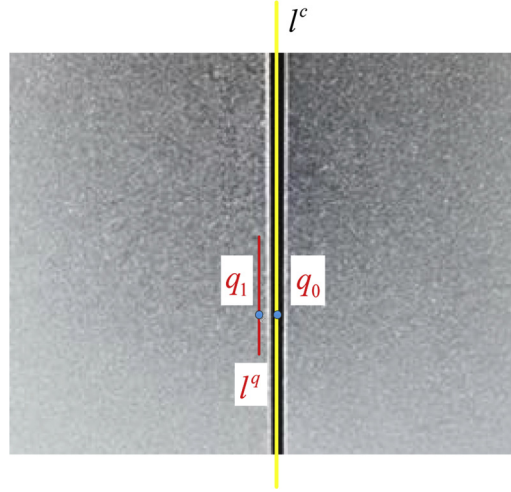


Fig. 6. Centerline of the seam and its parallel in image.

expressed as $P^{lq} = \{P_1^{lq}, P_1^{lq}, \dots, P_M^{lq}\}$. The least squares algorithm is used to fit P^{lq} into a spatial line, whose normal vector is recorded as $\mathbf{n}_{lq} = [a_{lq}, b_{lq}, c_{lq}]$.

Let q_1 be the nearest point to q_0 on the line l^q and Q_1 be the space point corresponding to q_1 , a space plane β with a normal vector \mathbf{n}_{lq} and passing Q_1 can be constructed, as shown in Fig.7. The pink dotted line in Fig.7 is the intersection of β with the plane α and γ on both sides of the seam, respectively. On both sides of the seam, points with a distance from plane β less than ε_d constitute a point set P , where ε_d is a preset distance threshold, usually 1–2 mm.

A new point set P' can be obtained by projecting the points in P onto β . The local coordinate system O-XYZ is established on the plane β so that the coordinate origin O is located on the plane β and the Z axis is perpendicular to the plane β . Those points in P' are transformed from camera coordinate system to local coordinate system O-XYZ, and the transformed point set is called as P'' . As shown in the red dot in Fig.8, the Z coordinate values of points in P'' are 0. In order to simplify the problem, only the X and Y coordinates are used for calculation in the later discussion.

According to Fig. 8, both D and G are two important inflection points. In order to obtain the width of the seam, it is critical to perform straight line fitting on the left point set and the right point set of the seam respectively, and separate D and G from the point set according to the distance of the point to the line. Define L_1 as the feature straight line of the left point set of the seam, that is, most of the points on the left point set are located on line L_1 , and the distance between point D and line L_1 is significantly larger than other points. Similarly, line L_2 can be defined as the feature straight line of the point set on the right side of the seam.

Define the coordinates of the i -th point in P'' as (x_i, y_i) , $i = 1, 2, \dots, N$, the adaptive piecewise straight line fitting of points in P'' can be expressed as follows

$$f(x) = \begin{cases} f_1(x) = k_1x + b_1, & x \in [x_1, x_r) \\ f_2(x) = k_2x + b_2, & x \in [x_r, x_s) \\ \dots & \dots \\ f_m(x) = k_mx + b_m, & x \in [x_t, x_n) \end{cases} \quad (5)$$

Where $f_i(x)$ ($i = 1, 2, \dots, n$) is the equation of the line for each segment, and m is the number of straight lines to which the point set P is

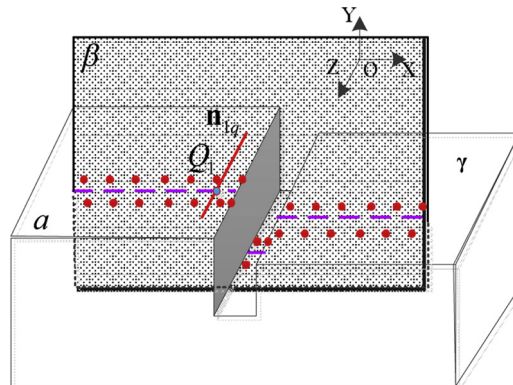


Fig. 7. Feature point set extraction for seam geometric analysis.

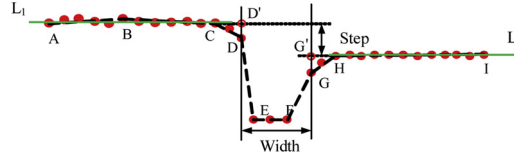


Fig. 8. Point cloud on O-XY plane.

fitted, which is automatically determined by the maximum fitting error is ε . ε is a preset empirical value, and its selection is mainly related to the accuracy of point cloud acquisition of the measurement equipment, which is usually 5 times of the average error of the measurement equipment. For example, the average measurement error of point cloud acquisition of the equipment used in this paper is about 0.01 mm, then ε is set to 0.05 mm.

Without loss of generality, assume AB, BC, ..., HI are the straight lines obtained by using Eq. (5) on the point set P", in order to find the straight line L_1 , starting from the straight line AB, the angle between two adjacent straight lines is calculated in turn. If the angle is less than the threshold value θ , the two adjacent lines are fused into a new straight line AC using a least squares fitting algorithm. Then use AC as the starting line to calculate the angle between it and the next adjacent line, and use a similar method to determine whether to merge with the next line. When the angle is greater than θ , the fusion process is terminated, and the final fused straight line is the desired L_1 . The θ is an empirical value and is usually set to 20° . Assume C is the right endpoint of the line L_1 . C is not necessarily the inflection point D because there may be chamfers at the seam boundary. Considering that the chamfer can be approximated by a straight line, we define the straight line CD which is adjacent to the straight line AC but does not satisfy the merge condition with AC as the straight line where the chamfer is located. Then, the left endpoint of the line CD is the inflection point D, and the projection D' of the point D on L_1 is considered as the ideal left boundary point of seam, as shown in Fig. 8. Similarly, a straight line L_2 and an ideal boundary point G' on the right side of the seam can be obtained. Thus, the height difference of the seam is defined as:

$$H_{gap} = \frac{d_{D'} + d_{G'}}{2} \quad (6)$$

$$d_{D'} = \frac{|A_2 x_{D'} + B_2 y_{D'} + C_2|}{\sqrt{A_2^2 + B_2^2}} \quad (7)$$

$$d_{G'} = \frac{|A_1 x_{G'} + B_1 y_{G'} + C_1|}{\sqrt{A_1^2 + B_1^2}} \quad (8)$$

where $d_{D'}$ and $d_{G'}$ are the distances from point D' to line L_2 and point G' to line L_1 , respectively. A_2 , B_2 , and C_2 are the equation coefficients of line L_2 , and A_1 , B_1 , and C_1 are the equation coefficients of the line L_1 , the height difference H_{gap} is defined as the average of the two distances.

The seam width can be defined as

$$W_{gap} = \frac{d_D + d_G}{2} \quad (9)$$

$$d_D = \frac{|A_4 x_D + B_4 y_D + C_4|}{\sqrt{A_4^2 + B_4^2}} \quad (10)$$

$$d_G = \frac{|A_3 x_G + B_3 y_G + C_3|}{\sqrt{A_3^2 + B_3^2}} \quad (11)$$

where d_D and d_G are the distances from point D to line GG' and from point G to line DD' respectively, A_4 , B_4 , C_4 and A_3 , B_3 , C_3 are the equation coefficients of the line GG' and DD' respectively, W_{gap} is defined as the average value of two distances.

In principle, along the length of the centerline of the seam, the height difference and width of each position are different. Therefore, in practical applications, a reasonable operation is to set a fixed step in the direction of the centerline to calculate the height difference and width of seam at different positions.

5. Visual display of detection results

Traditional detection methods usually display the results on a computer screen, and the position of the rivets and seams on the screen is not directly related to their physical position on the aircraft skin. Thus, the operators need to identify the corresponding relationship between the results and the physical rivets according to the imagination, and then use the pen to mark the results on the aircraft skin. Due to the strong self-similarity and huge number of rivets, it is easy for the operator to feel tired and make wrong labeling. To this end, this paper proposes a visualization method based on the augmented reality principle.

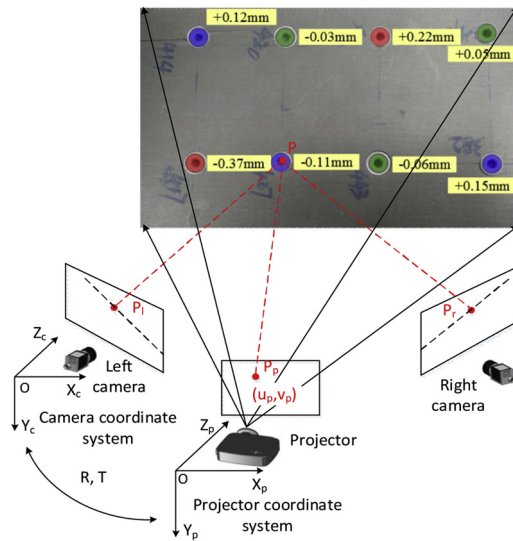


Fig. 9. Principle of visual display.

5.1. Principle of visual display

The basic principle of visual display is to associate the projection positions with the physical positions of the rivet and the seam, and use different colors to distinguish the error distributions. For example, as shown in Fig. 9, the red indicates that the height difference is seriously beyond the allowable threshold, blue indicates that it is slightly outside the allowable threshold, and green indicates that the height difference meets the requirements. In addition, the actual height difference value can be projected near each rivet area.

The key step to the method is to accurately project the geometric analysis results onto the detected area on the aircraft surface. As shown in Fig. 9, taking the measured point P in the space for analysis, its projection points in the left and right camera images are p_l and p_r respectively. According to the calibration result of the binocular vision system, the three-dimensional coordinate P_c of the point P in the left camera coordinate system can be obtained. If the transformation relationship between the projector coordinate system and the left camera coordinate system is known, the coordinates of the point P in the projector coordinate system can be found. According to the internal parameters of the projector obtained by the calibration, the projection point p_p of the point P on the image plane of the projector can be found. If a detection result (such as height difference, error color, etc.) is embedded near the p_p point of the projected image to create a new projection image, the detection result will be projected to the area near the P point on the aircraft surface, thereby realizing visual display of data processing results. In this method, the unknown parameters are the internal parameters of the projector, and the external parameters of the projector and the left camera. Therefore, the calibration of the projector parameters is the core problem of the method.

5.2. Projector calibration

Based on the principle of back projection, a calibration method of projector parameter based on high precision calibration board is proposed in this paper, as shown in Fig. 10. The calibration steps are as follows:

- (1) Let the projector project the pre-designed calibration pattern to the calibration plate (In Fig. 10, the red dots on the calibration plate represent the projection pattern, and the black dots are the pattern of the calibration plate itself.), and control the camera to take pictures of the calibration plate. The calibration plate pattern and the projection pattern can be separated by an image processing method, such as background subtraction technique.
- (2) The world coordinate system $OX_wY_wZ_w$ is established on the calibration board. According to the internal parameters of camera, the transformation matrix (R_c, t_c) of the world coordinate system $OX_wY_wZ_w$ relative to the camera coordinate system $OX_cY_cZ_c$ can be obtained.
- (3) The feature points of projection pattern are extracted from the camera image. According to the mathematical model of the camera and the constraints of the plane invariance of the calibration plate, the three-dimensional coordinates p_p of the feature points of the projection pattern in the world coordinate system $OX_wY_wZ_w$ are acquired.
- (4) The calibration plate is moved to obtain multiple images of projector pattern. Projector parameters can be calibrated using image feature points of the projected pattern and corresponding world coordinates by using the Zhang's calibration method [27].
- (5) After obtaining the internal parameters of the projector, the transformation matrix (R_c, t_c) between the left camera coordinate system and the current world coordinate system, the transformation matrix (R_p, t_p) between the projector coordinate system and the current world coordinate system can be calculated respectively for the calibration plate at any position. For any point p , if the

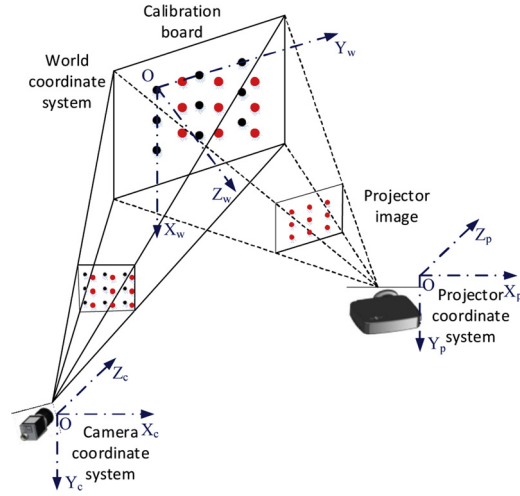
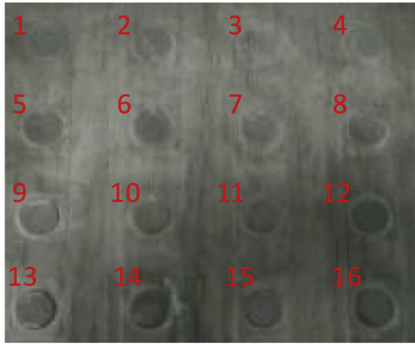


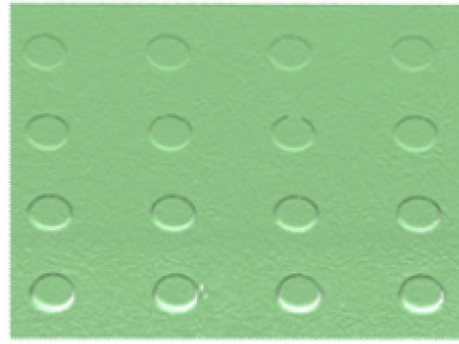
Fig. 10. Principle of projector calibration.



Fig. 11. Measurement system.



(a)



(b)

Fig. 12. Standard part with 16 rivets and scanned point cloud data.
 (a) Standard part; (b) Scanned point cloud data.

non-homogeneous coordinates of the point in the world coordinate system, left camera coordinate system and projector coordinate system are p_w , p_c and p_p , their relationship can be expressed as:

$$p_c = R_c p_w + t_c \quad (12)$$

$$p_p = R_p p_w + t_p \quad (13)$$

After eliminating p_w from the above formula, we can get:

$$p_p = R_p R_c^{-1} p_c + t_p - R_p R_c^{-1} t_c \quad (14)$$

Therefore, the transformation matrix between the projector and the camera can be expressed as

Table 1
Statistical measurement results of rivets' height difference.

	Ground truth (mm)	Measured value (mm)	Mean error (mm)	Standard deviation (mm)	Maximum error (mm)
Rivet 1	0.113	0.129	0.016	0.003	0.020
Rivet 2	0.143	0.144	0.001	0.002	0.005
Rivet 3	0.160	0.153	-0.007	0.001	0.009
Rivet 4	0.151	0.150	-0.001	0.002	0.003
Rivet 5	0.239	0.239	0.000	0.002	0.003
Rivet 6	0.257	0.249	-0.008	0.001	0.010
Rivet 7	0.265	0.247	-0.018	0.001	0.020
Rivet 8	0.254	0.244	-0.010	0.002	0.013
Rivet 9	0.533	0.536	0.004	0.002	0.006
Rivet 10	0.550	0.539	-0.011	0.003	0.015
Rivet 11	0.551	0.532	-0.019	0.003	0.023
Rivet 12	0.533	0.529	-0.004	0.004	0.009
Rivet 13	1.048	1.046	-0.002	0.003	0.007
Rivet 14	1.051	1.032	-0.019	0.003	0.023
Rivet 15	1.046	1.026	-0.020	0.003	0.024
Rivet 16	1.025	1.020	-0.004	0.002	0.007
Statistical average	-	-	0.009	0.0023	0.012

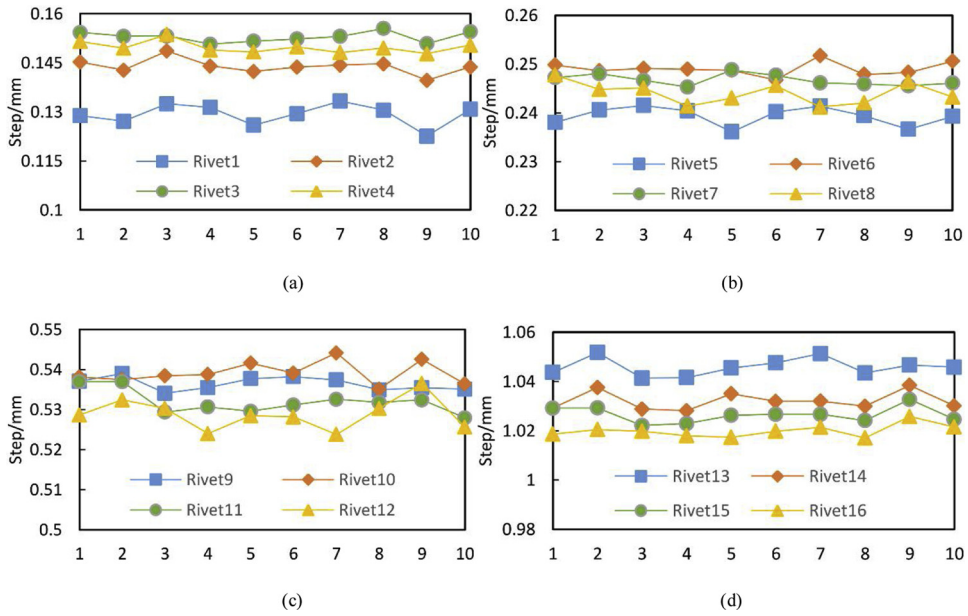


Fig. 13. Ten measurements of the height difference of each rivet.

$$R = R_p R_c^{-1} \quad (15)$$

$$t = t_p - R_p R_c^{-1} t_c \quad (16)$$

where R represents a 3×3 rotation matrix and t is a 3×1 translation matrix.

Up to now, the calibration of the projector has been completed. In this calibration method, feature point detection requires only a simple image processing algorithm, such as background subtraction, so it is hardly affected by the calibration pattern and ambient light, and is robust and efficient.

6. Experimental analysis

The experimental system is mainly composed of two industrial cameras, a projector and a computer. The developed prototype system is shown in Fig.11. The projector is a DLP projector from Texas Instruments with a resolution of 1280×800 and the cameras are CCD cameras with a resolution of 1624×1234 . In order to reduce the interference of ambient light, filters are installed in front of the lens. Cameras are connected to computers through Ethernet cables, and the DLP projector is connected to the computer via USB and HDMI. The camera and projector are fixed on the tripod by an adapter, which can realize arbitrary adjustment of three degrees of freedom. When the projector projects the grating images, it will trigger the left and right cameras to shoot synchronously.

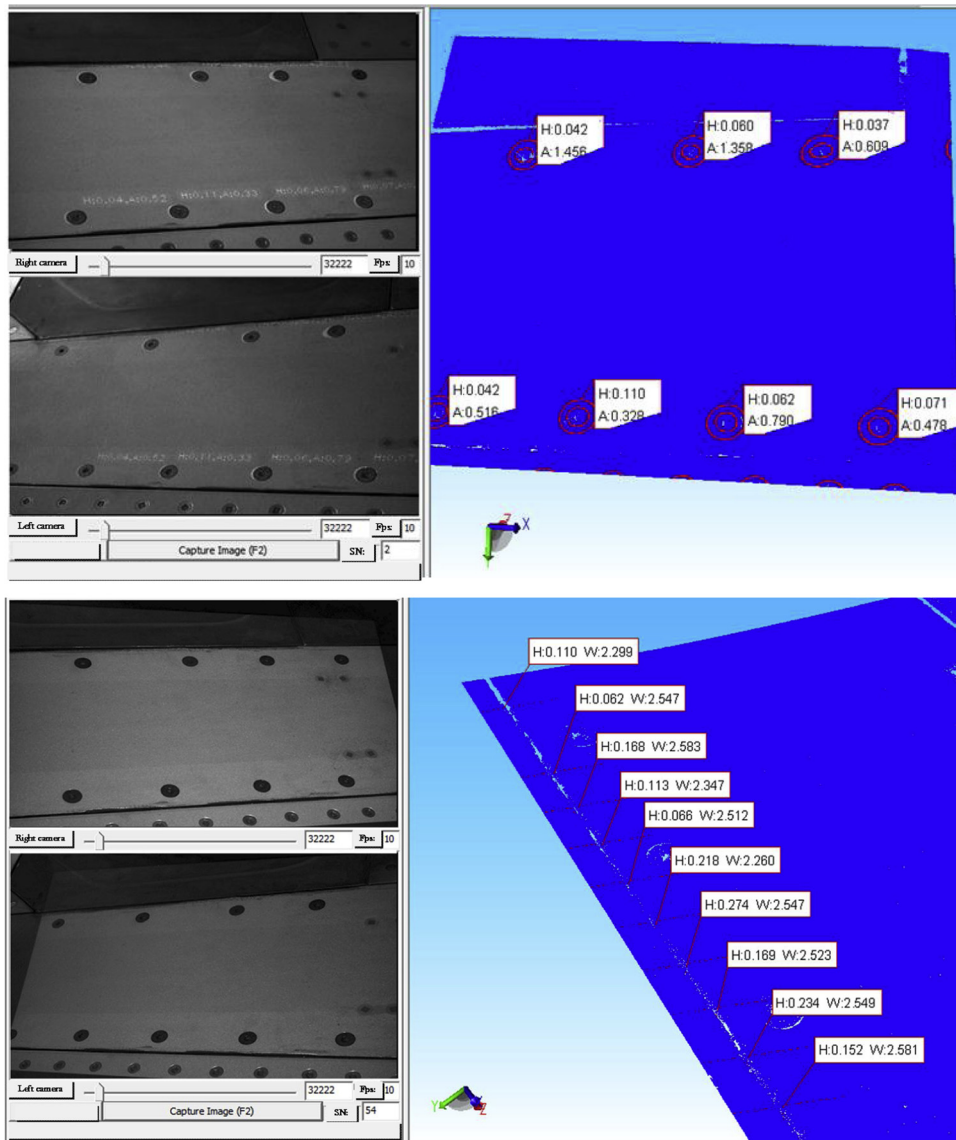


Fig. 14. Standard part with 16 rivets and scanned point cloud data.

Table 2

The measurements of rivets' height difference.

	Average value (mm)	Standard deviation (mm)	Maximum deviation (mm)
Rivet 1	0.046	0.006	0.020
Rivet 2	0.060	0.003	0.008
Rivet 3	0.048	0.005	0.019
Rivet 4	0.044	0.003	0.009
Rivet 5	0.109	0.003	0.009
Rivet 6	0.059	0.003	0.010
Rivet 7	0.071	0.004	0.015

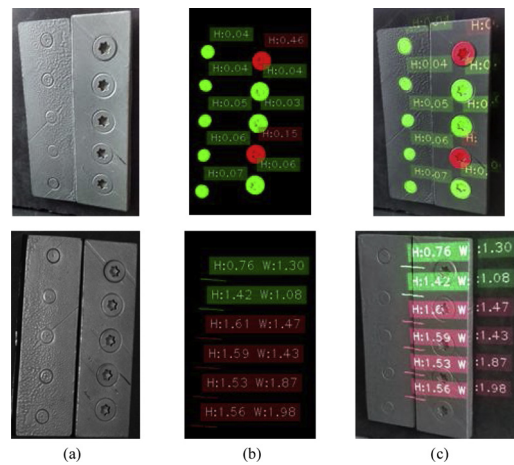
6.1. Accuracy analysis

In order to verify the accuracy of the developed inspection system, a standard part as shown in Fig. 12(a) was designed and machined. The standard part has 4 rows of rivets with different height differences, and the design values of the height differences are 0.1 mm, 0.2 mm, 0.5 mm and 1 mm from top to bottom. The height difference of each rivet is measured by a coordinate measuring

Table 3

The measurements of seam's height difference and width.

	step (mm)			width (mm)		
	Average value	Standard deviation	Maximum deviation	Average value	Standard deviation	Maximum deviation
Position 1	0.112	0.009	0.028	2.333	0.018	0.052
Position 2	0.064	0.005	0.015	2.562	0.016	0.045
Position 3	0.169	0.006	0.019	2.577	0.013	0.043
Position 4	0.110	0.006	0.020	2.356	0.013	0.041
Position 5	0.072	0.005	0.014	2.496	0.014	0.044
Position 6	0.216	0.006	0.019	2.270	0.017	0.050
Position 7	0.279	0.006	0.015	2.550	0.013	0.040
Position 8	0.164	0.006	0.018	2.536	0.012	0.038
Position 9	0.235	0.005	0.019	2.542	0.017	0.051
Position 10	0.157	0.007	0.018	2.567	0.013	0.038

**Fig. 15.** Results of visual display.

(a) Workpiece; (b) Image to be projected; (c) Detection result.

machine, and the measurement result is taken as a ground truth to participate in the subsequent comparison.

The system developed in this paper performs three-dimensional scanning on the standard parts, and the obtained point cloud data is shown in Fig. 12(b). Then the height difference of each rivet is calculated using the rivet detection algorithm proposed in this paper. The results of 10 scanning tests are given in Table 1, where the measured value refers to the average of 10 measurements of each rivet, and the mean errors refer to the difference between the ground truth and the average of 10 measurements. The maximum error refers to the maximum difference between the 10 measurements and the ground truth. It can be seen from Table 1 that the statistical mean error of height difference of the rivets is 0.009 mm, and the maximum error of the measurement result is 0.024 mm. Therefore, the proposed algorithm is relatively stable and has good accuracy. Fig. 13 shows the 10 measurements results of the height difference of each rivet.

6.2. Measurement of real parts

In order to verify the practicability of the proposed algorithm, rivets and seams are inspected on the real aircraft skin. As shown in Fig. 14, there are seven rivets and one seam in the measured area. Ten repetitive measurements were made and the measurement results are shown in Tables 2 and 3. The standard deviation in Table 2 indicates the degree of dispersion of the measurement results, and the maximum deviation indicates the maximum variation range of the measurement results. It can be seen that the standard deviation of the rivet height difference is within 0.006 mm, and the maximum deviation is within 0.02 mm. For the measurements of the seam area, the standard deviation of the height difference of seam is within 0.009 mm, the maximum deviation is 0.028 mm; the standard deviation of the seam width is within 0.018 mm, and the maximum deviation is within 0.052 mm. It can be seen from the above statistical results that the experimental system has good repeatability.

For engineering applications, efficiency is another important issue. For each scene on the aircraft skin, whose size is typically about 300 mm × 200 mm, the total time for measurement and data analysis of the developed system is approximately 8 s, which is sufficient for practical applications.

In order to show the effectiveness of the proposed visualization method more intuitively, we give a colored example, as shown in Fig. 15. The experimental results show that the proposed method can accurately project the detection results onto the physical surface

of the measured part, which can greatly improve the operation efficiency of workers. Therefore, the measurement method has significant practical value.

7. Conclusion

In this paper, we propose a new method for manufacturing quality detection of aircraft surface based on fringe projection. To reduce phase errors, an improved fringe projection measurement method was introduced to enhance the adaptability of the method to free-form surfaces such as aircraft surfaces. A new method for calculating the height difference and width of seams based on image and point cloud data fusion is proposed. Finally, in order to facilitate the labeling of detection results, a method for visualizing detection results based on augmented reality is proposed. The experimental results show that the average measurement error of the rivet height difference is about 0.009 mm, which proves that the method has good accuracy. At present, the main problem is that the proposed method is mainly aimed at manufacturing defects related to rivets and seams, and cannot be directly applied to other kinds of defects. However, the proposed method gives a new detection mechanism, which has good potential for expansion. In the future, we will optimize the algorithm for the practical application and develop a more efficient detection system to meet the needs of online testing. In addition, the installation of this device on the articulated robot enables a more flexible inspection application.

Declaration of Competing Interest

The authors declare that they have no known competing financial interests or personal relationships that could have appeared to influence the work reported in this paper.

Acknowledgments

This work was supported by the National Key R&D Program of China under Grant No. 2018YFB1107800, the Key projects of major research program of NSFC under Grant No. 91948203, and the National Natural Science Foundation of China under Grant No. 51805527. The authors would like to thank the anonymous referees for their valuable suggestions and comments.

References

- [1] A.K. Kundu, S. Raghunathan, R.K. Cooper, Effect of aircraft surface smoothness requirements on cost, *Aeronaut. J.* 104 (2000) 415–420.
- [2] M.Z. Gong, P.J. Yuan, T.M. Wang, L.B. Yu, H.W. Xing, W. Huang, A novel method of surface-normal measurement in robotic drilling for aircraft fuselage using Three laser range sensors, *IEEE/ASME International Conference on Advanced Intelligent Mechatronics* (2012) 321–324.
- [3] F. Salazar, A. Barrientos, Surface roughness measurement on a wing aircraft by speckle correlation, *Sensors* 13 (2013) 11772–11781.
- [4] B. Jang, M. Kim, J. Park, S. Lee, Design optimization of composite radar absorbing structures to improve stealth performance, *Int. J. Aeronaut. Space Sci.* 17 (2016) 20–28.
- [5] R. Panwar, J.R. Lee, Performance and non-destructive evaluation methods of airborne radome and stealth structures, *Meas. Sci. Technol.* 29 (2018).
- [6] M. Siegel, P. Gunatilake, G. Podnar, Robotic assistants for aircraft inspectors, *Ind. Rob.* 25 (1998) 389–+.
- [7] Z. Liu, D.S. Forsyth, A. Marincak, P. Vesley, Automated rivet detection in the EOL image for aircraft lap joints inspection, *Ndt E Int.* 39 (2006) 441–448.
- [8] J.H. Wang, M.R. Wang, Handheld non-contact evaluation of fastener flushness and countersink surface profiles using optical coherence tomography, *Opt. Commun.* 371 (2016) 206–212.
- [9] P.H. Allard, J.A. Lavoie, J.S. Fraser, Improvement of aircraft mechanical damage inspection with advanced 3D imaging technology, *The 5th International Symposium on NDT in Aerospace* (2013).
- [10] G. Georgeson, Trends in R&D for Nondestructive Evaluation of In-Service Aircraft, *The 5th International Symposium on NDT in Aerospace* (1996).
- [11] W.W. Zhang, B.H. Zhuang, Non-contact measurement of scratches on aircraft skins and windows, in: K.G. Harding, D.J. Svetkoff (Eds.), *Three-Dimensional Imaging and Laser-Based Systems for Metrology and Inspection III*, 1997, pp. 90–94.
- [12] Z.Y. Feng, Airworthiness responsibility analysis of aircraft manufacturer based on investigation of aloha accident, *2009 International Symposium on Aircraft Airworthiness* (2009).
- [13] S.L. Chen, R.B. Xia, J.B. Zhao, H.Y. Zhang, M.B. Hu, Analysis and reduction of phase errors caused by nonuniform surface reflectivity in a phase-shifting measurement system, *Opt. Eng.* 56 (2017).
- [14] B. Pan, Q. Kemao, L. Huang, A. Asundil, Phase error analysis and compensation for nonsinusoidal waveforms in phase-shifting digital fringe projection profilometry, *Opt. Lett.* 34 (2009) 416–418.
- [15] S. Zhang, P.S. Huang, Phase error compensation for a 3-D shape measurement system based on the phase-shifting method, *Opt. Eng.* 46 (2007).
- [16] C. Waddington, J. Kofman, Camera-independent saturation avoidance in measuring high-reflectivity-variation surfaces using pixel-wise composed images from projected patterns of different maximum gray level, *Opt. Commun.* 333 (2014) 32–37.
- [17] L. Ekstrand, S. Zhang, Three-dimensional profilometry with nearly focused binary phase-shifting algorithms, *Opt. Lett.* 36 (2011) 4518–4520.
- [18] F. Mai, Y.S. Hung, H. Zhong, W.F. Sze, A hierarchical approach for fast and robust ellipse extraction, *Pattern Recognit.* 41 (2008) 2512–2524.
- [19] L. Libuda, I. Grothues, K.F. Kraiss, Ellipse detection in digital image data using geometric features, in: J. Braz, A. Ranchordas, H. Araujo, J. Jorge (Eds.), *Advances in Computer Graphics and Computer Vision*, 2007 pp. 229–+.
- [20] A.Y.S. Chia, S. Rahardja, D. Rajan, M.K. Leung, A Split and Merge Based Ellipse Detector With Self-Correcting Capability, *IEEE Trans. Image Process.* 20 (2011) 1991–2006.
- [21] Y.H. Xie, Q. Ji, A new efficient ellipse detection method, in: R. Kasturi, D. Laurendeau, C. Suen (Eds.), *16th International Conference on Pattern Recognition, Vol II, Proceedings*, 2002, pp. 957–960.
- [22] A.Y.S. Chia, M.K.H. Leung, H.L. Eng, S. Rahardja, *IEEE, ellipse detection with Hough transform in one dimensional parametric space*, 2007 *Ieee International Conference on Image Processing Vol. 1–7* (2007) pp. 2585–+.
- [23] W. Lu, J.L. Tan, Detection of incomplete ellipse in images with strong noise by iterative randomized Hough transform (IRHT), *Pattern Recognit.* 41 (2008) 1268–1279.
- [24] S.L. Chen, R.B. Xia, J.B. Zhao, Y.L. Chen, M.B. Hu, A hybrid method for ellipse detection in industrial images, *Pattern Recognit.* 68 (2017) 82–98.
- [25] C. Steger, Extracting curvilinear structures: a differential geometric approach, *European Conference on Computer Vision* (1996).
- [26] C. Steger, An unbiased detector of curvilinear structures, *IEEE Trans. Pattern Anal. Mach. Intell.* 20 (1998) 113–125.
- [27] Z.Y. Zhang, A flexible new technique for camera calibration, *IEEE Trans. Pattern Anal. Mach. Intell.* 22 (2000) 1330–1334.